Solution-Processed Ternary Tin (II) Alloy as Hole-Transport Layer of Sn–Pb Perovskite Solar Cells for Enhanced Efficiency and Stability

*Zhenhua Yu, Jiantao Wang, Bo Chen, Md Aslam Uddin, Zhenyi Ni, Guang Yang, and Jinsong Huang**

Tin–lead (Sn–Pb) narrow-bandgap (NBG) perovskites show great potential in both single-junction and all-perovskite tandem solar cells. Sn–Pb perovskite solar cells (PSCs) are still limited by low charge collection efficiency and poor stability. Here, a ternary Sn (II) alloy of SnOCl is reported as the hole-transport material (HTM) with a work function of 4.95 eV for Sn–Pb PSCs. The solution-processed SnOCl layer has a texture structure that not only reduces the optical loss of the devices, but also changes grain growth of Sn–Pb perovskites and boosts the carrier diffusion length to 3.63 µm. The formation of small perovskite grains at the HTM/perovskite interface is suppressed. These result in an almost constant internal quantum efficiency (IQE) of 96 ± 2% across the absorption spectrum of Sn–Pb perovskites. The SnOCl HTM significantly enhances the stability of Sn–Pb PSCs with 87% of its initial efficiency retained after 1-sun illumination for 1200 h, and keeps 85% efficiency under 85 °C thermal stress for 1500 h. The hybrid HTM further improves the stabilized efficiencies of single-junction Sn–Pb PSCs and all-perovskite tandem solar cells to 23.2% and 25.9%, respectively. This discovery opens an avenue to the multicomponent metal alloys as HTM in PSCs.

1. Introduction

Metal halide perovskites have attracted tremendous attention as promising photovoltaic materials in solar cells, with a rapidly boosted power conversion efficiency (PCE) reaching 25.7% for single-junction perovskite solar cells (PSCs) in the past decade.[1–7] The efficiency of multijunction tandem solar cells has the potential to exceed the thermodynamic limit of single-junction devices. The broad tunability of perovskite bandgap between 1.2 and 3.2 eV, by varying their iodine (I)/bromine (Br) or tin (Sn)/lead (Pb) ratio, makes them good candidates for the multijunction architectures,[8–12] such as organic/perovskite, silicon/perovskite or Cu(In, Ga)Se_2 (CIGS)/perovskite double-junction tandem solar cells.[13–15] A narrow-bandgap (NBG) perovskite of 1.21 eV can be obtained by replacing 50 mol% of Pb with Sn, which is a promising candidate for the NBG subcell in tandem cells. All-perovskite tandem solar cells consisting of the Sn–Pb NBG perovskite and a wide-bandgap (WBG) perovskite with a bandgap of 1.75–1.80 eV in general, can have a maximum efficiency of over 30%. All solution fabrication processes for all-perovskite tandem solar cells make it with great potential to retain the low-fabrication cost merit of perovskites.[16,17] Thus, all-perovskite tandem solar cells are attracting increasing attention and have a rapid improvement of PCE in recent years,[18–21] and the reported record PCE has already gone beyond that of single-junction perovskite cells.[22]

The performance of Sn–Pb perovskite NBG perovskite subcells is still limiting the performance of all-perovskite tandem solar cells. The best reported short-circuit current density (J_{SC})[23] is still short of the value by assuming an external quantum efficiency (EQE) of 90% across the whole absorption spectrum. The poor stability of Sn–Pb NBG perovskites is an even bigger problem shadowing the prospect of all-perovskite tandem solar cells.[22,24] Besides the easy oxidation of Sn^{2+} in Sn–Pb perovskites,[25] a recent study by Haque et al. showed that the formation of iodine also exists in iodide-based Sn–Pb perovskites, limiting their photostability.[26] Recent studies showed the most-commonly used hole-transport material (HTM) for Sn–Pb perovskite solar cells, poly(3,4-ethylenedioxythiophene):poly(styrenesulfonate) (PEDOT:PSS), which resulted in the highest reported efficiency in the literature,[27,28] also participates in the degradation of Sn–Pb perovskite. Proton from acidic PEDOT:PSS accelerates the oxidization of iodide into iodine which further oxidize Sn^{2+} and generates enormous damage as evidenced by a notable morphologic change of Sn–Pb perovskites.[29] HTM-free devices have been demonstrated to be significantly more stable, indicating that the bottom contact of the Sn–Pb PSCs is crucial to the stability of devices.

Z. Yu, J. Wang, B. Chen, Md A. Uddin, Z. Ni, G. Yang, J. Huang
Department of Applied Physical Sciences
University of North Carolina
Chapel Hill, NC 27599, USA
E-mail: jhuang@unc.edu

J. Huang
Department of Chemistry
University of North Carolina at Chapel Hill
Chapel Hill, NC 27599, USA

The ORCID identification number(s) for the author(s) of this article can be found under https://doi.org/10.1002/adma.202205769.

DOI: 10.1002/adma.202205769

New HTMs for PSCs,[30,31] especially the Sn–Pb PSCs are urgently desired. Nickel oxides were explored as a potential candidate despite high annealing temperatures,[32] and reaction with methylamine (MA^+) cations.[33] The efficiency of NBG devices using nickel oxides are still inferior to those using PEDOT:PSS. We recently found that a mixed valence tin oxide (SnO_{2-x}) fabricated at low-temperature by atomic layer deposition (ALD) could be a suitable HTM for Sn–Pb PSCs, leading to an efficiency close to those made of PEDOT:PSS.[21] The main advantage of using SnO_{2-x} as the HTM for Sn–Pb PSCs comes from a greatly enhanced device stability. However existing ALD processes are still expensive, and have low throughput, and nonuniformity issues could arise when one needs to increase the size of perovskite modules. This motivated us to look for new solution-processed tin oxides.

Herein, we report a ternary Sn (II) alloy of SnOCl to replace the PEDOT:PSS as the HTM in Sn–Pb PSCs. The SnOCl could be easily fabricated by solution process followed by a brief annealing at 100°C. The optimized SnOCl HTM has a textured morphology, reducing the optical loss of the device. In addition, the Sn–Pb perovskite film growth on SnOCl did not form small grains on the bottom of the films, unlike that in PEDOT:PSS based devices, resulting in an increased carrier diffusion length of 3.63 µm. The devices using SnOCl HTM have a notably increased J_{SC} of >32 mA cm^{-2} and high efficiency of 22.2%. Additionally, the SnOCl HTM greatly enhances the long-term stability of the Sn–Pb PSCs. The best devices retained 87% of the initial efficiency after light soaking under 1-sun illumination for 1200 h, and retain 85% of the initial efficiency after heating at 85 °C for 1500 h. The hybrid neutral PEDOT/SnOCl HTM can further improve the efficiency of Sn–Pb PSCs to 23.2%, which also effectively increased the J_{SC} of all-perovskite tandem solar cells to over 16 mA cm^{-2} with a high efficiency of 26.3% (stabilized 25.9%).

2. Sn(II)OCl HTM for Sn–Pb PSCs

Tin (II) chloride ($SnCl_2$) is a commonly used precursor to synthesize SnO or SnO_2 by solution process, depending on the conditions of the O_2, H_2O, PH value, and temperature.[34] To design a proper HTM for Sn–Pb PSCs, a p-type Sn(II) O-dominated alloy is needed. Thus, we chose to dissolve $SnCl_2$ in ethanol with ≈0.1 vol% water, and fabricate the HTM in a N_2-filled glovebox to avoid the formation of SnO_2. We tuned the PH value of $SnCl_2$ solution by adding sodium hydroxide (NaOH), and tuned the annealing temperature from room temperature (RT) ≈25 °C to 150 °C. We evaluated these HTMs made at different conditions using Sn–Pb PSCs. The results shown in Figure S1a,b (Supporting Information) show that the best efficiency of Sn–Pb PSCs was achieved with the precursor solution PH value of 10 and the annealing temperature of 100 °C. To find out the composition of the HTM, X-ray diffraction (XRD) and X-ray photoelectron spectroscopy (XPS) measurements were conducted. As shown in **Figure 1**a, the new HTM is amorphous. The XRD pattern only shows a weak peak at 11.5 °, which is very different from those of SnO or SnO_2.[35] As shown in Figure 1b, the derived composition of the as-prepared film from XPS measurement is $SnO_{0.93}Cl_{1.12}$. We speculate it may still contain some unreacted $SnCl_2$. Since $SnCl_2$ is highly soluble in perovskite precursor solvents of DMF and DMSO, while tin oxides are not, we can thus separate $SnCl_2$ and the oxides by washing off $SnCl_2$ using these solvents. After washing the $SnCl_2$ residual away from the film by immersing the films in DMF/DMSO (3:1 in volume) for 10 min, the HTM shows a composition of $SnO_{0.91}Cl_{0.22}$. The $SnO_{0.91}Cl_{0.22}$ fabricated by the optimal conditions is denoted as SnOCl hereafter to represent the ternary tin (II) alloy HTM. We can thus infer that ≈90% of Sn ions in SnOCl are divalent Sn^{2+}. Our previous computation showed that the hybridization of O 2p and Sn 5s orbitals of SnO introduced mid-gap states which enables hole transport properties of SnO_{2-x}. A large percentage of SnO (≈90%) in this new HTM should enlarge Sn–O–Sn angles and increase orbital overlapping between O and Sn atoms, contributing to an improved hole conduction capability. The Fermi level of the SnOCl was determined by ultraviolet photoelectron spectroscopy (UPS) measurement. The SnOCl has a work function of 4.95 eV (Figure S2, Supporting Information), which is close to that of PEDOT:PSS and thus proper for HTM in Sn–Pb PSCs. The SnOCl also has the conductivity of 2.7×10^{-3} S cm^{-1} and the mobility of 7.4×10^{-2} cm^2 V^{-1} s^{-1} (Table S1, Supporting Information).

We optimized the thickness of the SnOCl by tuning the concentration of $SnCl_2$. Figure S3 (Supporting Information) shows that the 0.1 M $SnCl_2$ resulted in the best PCE for Sn–Pb PSCs. We thus compared the optimized SnOCl with the most-commonly used PEDOT:PSS in the same batch of Sn–Pb PSCs. As shown in Figure 1c and **Table 1**, the SnOCl HTM boosted efficiency to 21.4 ± 0.4%, when PEDOT:PSS resulted in an efficiency of 20.3 ± 0.3%. The PCE enhancement is mostly from the increased J_{SC} from 31.0 ± 0.1 mA cm^{-2} to 32.1 ± 0.2 mA cm^{-2}. SnOCl based champion Sn–Pb device showed high efficiency of 22.2% with an open-circuit voltage (V_{OC}) of 0.85 V, a J_{SC} of 32.3 mA cm^{-2} and a fill factor (FF) of 80.4%, as shown in Figure 1d. **Figure 2**a exhibits the EQE spectra of the champion Sn–Pb PSCs using PEDOT:PSS and SnOCl HTMs, respectively. Their integrated J_{SC} is 30.2 and 31.8 mA cm^{-2}, respectively, agreeing well with *J–V* results shown in Figure 1d.

2.1. The Optoelectronic Properties of SnOCl HTM for Sn–Pb PSCs

We noticed that the Sn–Pb PSC device with SnOCl changed the shape of EQE spectra. In addition to the enhanced EQE in the long wavelength range, there is a shifting of the EQE peak in shorter wavelength range from 350 to 520 nm, which might be caused by the optical effect from the new HTM. To understand it, we compared the reflection spectra of the devices using PEDOT:PSS and SnOCl. As shown in Figure 2a, the PEDOT: PSS-based device has a stronger reflection ranging from 450 to 750 nm, agreeing well with the EQE results. This part of optical loss may be due to the light absorption of PEDOT:PSS and the light reflection at the ITO/PEDOT:PSS/perovskite interfaces. In addition, we found the optimized SnOCl has a texture-like morphology as shown by the top-view and cross-sectional view SEM images in Figure 2b and Figure S4a (Supporting Information). As shown in Figure S4

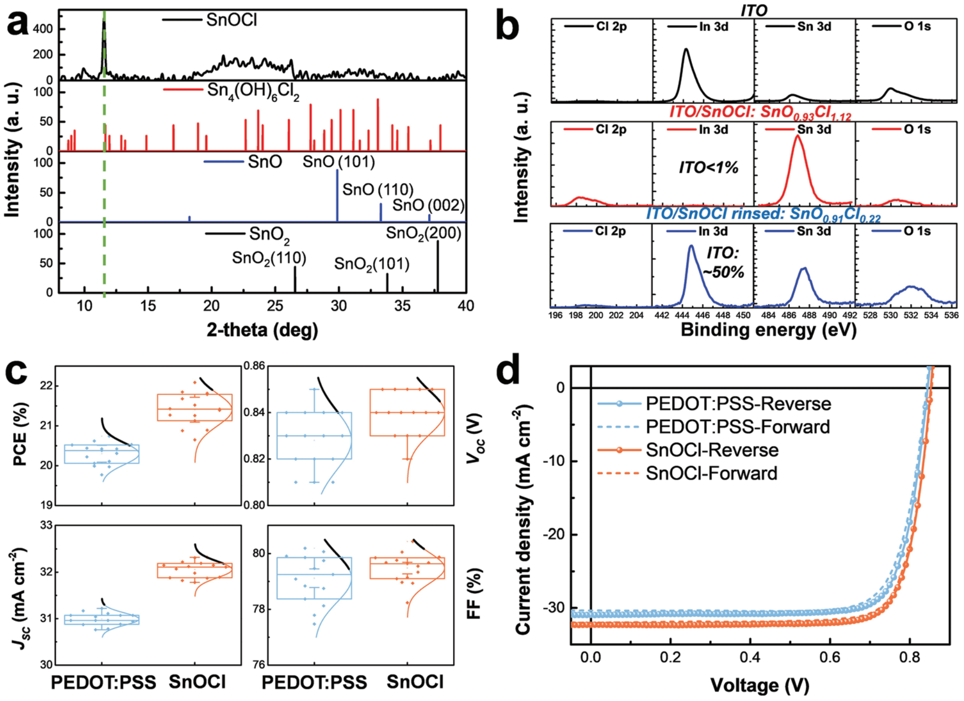

Figure 1. Ternary Sn (II) alloy of SnOCl as the HTM for Sn–Pb PSCs. a) XRD pattern for SnOCl powders compared with standard XRD patterns for $Sn_4(OH)_6Cl_2$, SnO, and SnO_2. The SnOCl films after rinsing by DMF/DMSO were scraped off to collect SnOCl powders for XRD measurement. b) XPS spectra for Cl, In, Sn, and O of ITO, ITO/SnOCl (pristine), and ITO/SnOCl (washed by DMF/DMSO), respectively. c) PV parameters statistics for Sn–Pb PSCs using PEDOT:PSS and SnOCl as HTMs, respectively. 15 devices for each type of HTM are fabricated for statistics. d) *J*–*V* curves under reverse and forward scanning for the champion Sn–Pb PSCs with PEDOT:PSS and SnOCl as HTMs. The PV parameters for all the Sn–Pb PSCs (8 mm^2 device area with a 5.9 mm^2 photomask) were determined by the *J*–*V* measurements under reverse scanning at 0.05 V s^{-1}.

(Supporting Information), the concentration of $SnCl_2$ solution determines the morphology of the SnOCl films, including the size of the pyramids and the spacing between them. For the optimized concentration of 0.1 M $SnCl_2$ which resulted in the highest device efficiency, the SnOCl HTM shows pyramids with a height of ≈300 nm, diameter of ≈1 µm and spacing of ≈2 µm. We also confirmed that the areas between pyramids were covered by a thin (≈20 nm) layer of SnOCl nanoparticles by examining the tilted view SEM image of a typical sample (Figure S5, Supporting Information), therefore Sn–Pb perovskites do not contact ITO directly. Keeping the wet SnOCl on ITO substrate at room temperature for 5 min before annealing is found to effectively form the texture structure of SnOCl HTM. Based on the studies above, a possible formation process for the texture structure is illustrated in Figure S6 (Supporting Information).

This texture structure should cause the SnOCl HTM to have the functions of light anti-reflection or scattering in Sn–Pb PSCs without leading to notable change of the perovskite layer (Figure S7, Supporting Information), similar to the textured structures in silicon solar cells.[36] To test this hypothesis, we compared the SnOCl HTMs made of 0.02 M and 0.1 M $SnCl_2$, respectively, to tune the texture morphology. For the SnOCl made of a very low concentration of 0.02 M $SnCl_2$, almost no pyramids could be found but there was a SnOCl thin layer in the cross-sectional SEM, as shown in Figure 2b. As shown in Figure 2c, the device with textured SnOCl (0.1 M $SnCl_2$) shows slightly enhanced EQE and reduced reflection

Table 1. Photovoltaic parameters for single-junction and all-perovskite tandem solar cells. HTMs without special statements here refer to the single-junction narrow-gap (1.21 eV) PSCs using varied HTMs, WBG refers to the wide-gap perovskite with a bandgap of 1.75 eV. All the solar cells reported in this work are fabricated with work areas of 8 mm^2 and measured with 5.9 mm^2 photomask.

	PCE [%]	V_{OC} [V]	J_{SC} [mA cm^{-2}]	FF [%]	τ [µs]	μ [cm^2 V^{-1} s^{-1}]	D_L [µm]
PEDOT:PSS (Champion cell)	20.3 ± 0.3 (20.7)	0.83 ± 0.01 (0.84)	31.0 ± 0.1 (31.0)	79.1 ± 0.9 (79.7)	1.34	1.35	2.15
SnOCl (Champion cell)	21.4 ± 0.4 (22.2)	0.84 ± 0.01 (0.85)	32.1 ± 0.2 (32.3)	79.5 ± 0.5 (80.4)	2.07	2.45	3.63
Hybrid neutral PEDOT/SnOCl Champion cell	23.2	0.89	32.2	80.9			
WBG cells (Champion cell)	17.3 ± 0.3 (17.7)	1.22 ± 0.02 (1.24)	17.9 ± 0.2 (18.1)	79.4 ± 1.0 (78.9)			
Tandem cells-PEDOT:PSS (Champion cell)	24.6 ± 0.4 (25.2)	2.02 ± 0.01 (2.04)	15.6 ± 0.2 (15.7)	78.1 ± 1.0 (78.9)			
Tandem cells-PEDOT/SnOCl (Champion cell)	25.2 ± 0.7 (26.3)	2.03 ± 0.02 (2.05)	16.0 ± 0.2 (16.2)	77.6 ± 1.0 (79.3)			

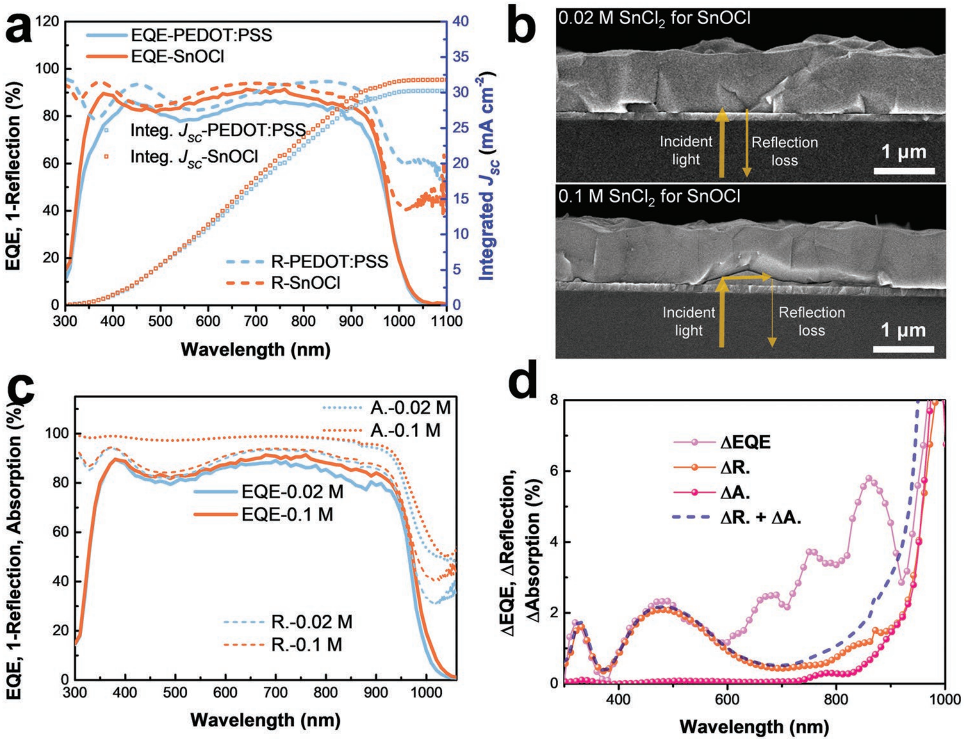

Figure 2. Optical properties for SnOCl-based Sn–Pb PSCs. a) The reflection spectra, EQE spectra and integrated J_{SC} for the champion Sn–Pb PSCs using PEDOT:PSS and SnOCl as HTMs, respectively. Their integrated J_{SC} is 30.7 and 31.8 mA cm^{-2}, respectively. The devices for the reflection test were the same size (1.5 cm × 0.7 cm) and fully covered by copper electrodes. The reflection measurements were taken using an integrating sphere. b) Cross-section SEM images for perovskites on SnOCl HTMs made of 0.02 M and 0.1 M SnCl$_2$, respectively. c) EQE, reflection (*R.*) and absorption spectra for PSCs using SnOCl HTMs made of 0.02 M and 0.1 M SnCl$_2$, respectively. d) The difference of EQE (ΔEQE: EQE$_{0.1M}$ − EQE$_{0.02M}$), reflection (Δ*R.*: Reflection$_{0.02M}$ − Reflection$_{0.1M}$), and the absorption (Δ*A.*: Absorption$_{0.1M}$ − Absorption$_{0.02M}$) spectra between Sn–Pb PSCs using SnOCl made of 0.02 M and 0.1 M SnCl$_2$, respectively. The dashed line refers to Δ*R.* + Δ*A.*.

in the wavelength range from 400 to 1000 nm, and a slightly enhanced absorption from 850 to 1000 nm compared to the device without textured SnOCl (0.01 M SnCl$_2$). To make the comparison clear, we plotted the difference of the EQE (ΔEQE), reflection (ΔR.) and absorption (ΔA.) spectra of perovskite films with these two SnOCl HTMs in Figure 2d for a direct comparison. The reflection difference (ΔR.) matched well with their EQE difference (ΔEQE) in the wavelength range from 300 to 600 nm, indicating the optimized SnOCl texture structure did have an anti-reflection function in Sn–Pb PSCs. We cannot exclude the light scattering effect of the optimized SnOCl due to the irregular shape of pyramids, but its contribution to the EQE increase ranging 750 to 1000 nm is limited. However, the changes of perovskite absorption and/or the reflection from the device induced by the textured HTM are still too small to explain the large change of EQE, as illustrated by the dash line in Figure 2d.

To understand whether the contribution of EQE change comes from change of perovskite property, we compared the internal quantum efficiency (IQE) spectra of Sn–Pb PSCs with PEDOT:PSS and SnOCl as HTMs, respectively. Here we assume 1 − *R* represents the total absorption of the light by the devices, though it should still include some optical loss due to parasitic absorption in the devices. As shown in **Figure 3**a, the PEDOT: PSS-based device has notable IQE loss in both blue (360–550 nm) and red (750–950 nm) regions, while the SnOCl based device has an almost constant of 96 ± 2% within the whole absorption spectrum ranging from 360 to 950 nm. This indicates the Sn–Pb perovskites deposited on SnOCl have better charge collection efficiency. The carrier-recombination lifetime in Sn–Pb PSCs using PEDOT:PSS and SnOCl HTMs were measured by transient photovoltage decay (TPV) under one sun light bias. As shown in Figure 3b and Figure S8 (Supporting Information), the Sn–Pb PSC with SnOCl HTM not only showed large V_{OC}, but also a longer TPV lifetime of 2.07 µs.[37] It is noted that the measured carrier-recombination lifetime in TPV measurement is about ten times larger than the capacitance discharge lifetime, making this measurement valid. This is confirmed by the time-resolved photoluminescence (TRPL) results in Figure S9 (Supporting Information) showing an enhancement of radiative carrier-recombination lifetime caused by SnOCl. We thus measured carrier mobilities of Sn–Pb perovskites using PEDOT:PSS and SnOCl HTMs by transient photocurrent decay (TPC), in which light came into perovskites from copper and ITO side for the electron and hole mobility measurement, respectively.[38] As shown in Figure 3c and Figure S10 (Supporting Information), Sn–Pb perovskites deposited on PEDOT:PSS and SnOCl have electron mobilities of 1.35 and 2.45 cm^2 V^{-1} s^{-1}, respectively, while they have similar hole mobilities of over 4.5 cm^2 V^{-1} s^{-1}. Thus, SnOCl leads to an increased electron diffusion length of 3.63 µm for Sn–Pb PSCs, compared to 2.15 µm for PEDOT:PSS. A longer charge

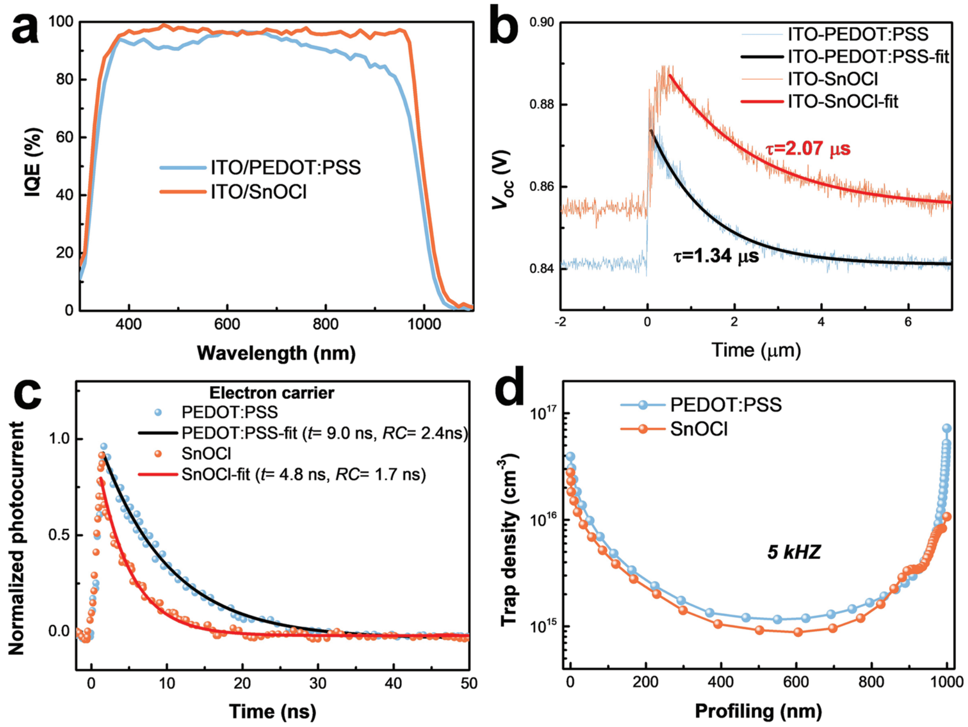

Figure 3. Electronic properties for SnOCl-based Sn–Pb PSCs. a) IQE spectra for the champion Sn–Pb PSCs using PEDOT:PSS and SnOCl as HTMs, respectively. b) TPV and c) TPC with biexponential fits for Sn–Pb PSCs using PEDOT:PSS and SnOCl as HTMs, respectively. To measure the electron mobility of the devices by TPC, the incident light is illuminated from the copper electrode (30 nm) side. d) DLCP measurements taken at 5 kHz for Sn–Pb PSCs using PEDOT:PSS and SnOCl as HTMs, respectively.

diffusion length thus allows more efficient collection of photogenerated carriers. This is particularly important for charge carriers generated by longer wavelength light which distribute through the perovskite films due to the weaker light absorption in this wavelength range, which explains the higher IQE in the long wavelength range.

To understand the different IQE in short wavelength range for the devices with different HTMs, we conducted the drive-level capacitance profiling (DLCP) measurement to Sn–Pb PSCs based on PEDOT:PSS and SnOCl at a relatively low ac frequency of 5 kHz, which mainly reflects the spatial distribution of traps with high depths of <0.4 eV. As shown in Figure 3d, the trap density in Sn–Pb perovskites near HTM is ten times higher in the PEDOT:PSS based device than in the SnOCl device. This explains the loss of IQE at short wavelength range in PEDOT:PSS based devices, because UV and blue light have short penetration depths. To further investigate the origin of the very high trap density in PEDOT:PSS based devices, we measured the morphology of the perovskite films using cross-sectional scanning electron microscopy (SEM). By comparing the SEM images of perovskites close to the PEDOT:PSS/perovskite and the SnOCl/perovskite interfaces, we found a large density of small grains near the PEDOT:PSS/perovskite interface, but they do not exist for the perovskite deposited on SnOCl, as shown in Figure S11 (Supporting Information). As shown in Figure S7 (Supporting Information), the crystallization of Sn–Pb perovskite films deposited on SnOCl HTMs is slightly better than that on PEDOT:PSS. The much larger surface area of these small grains may contribute to the very high trap density in perovskites close to this interface. As reported in our previous work, perovskite generally nucleates from film surface due to the quick evaporation of solvent from the film surface.[24] However, in the case of PEDOT:PSS as HTM, the very strong interaction of the sulphate group to Pb may lead to additional nucleation near the HTM side, and this can be notable when the film is so thick that it takes longer for solvents to leave the film during drying. This may induce the formation of a large density of small grains near the PEDOT:PSS/perovskite interface. Additional evidence that the large density traps in the small-grained layer comes from the study of photoluminescence (PL) of the perovskite films with incident light from ITO or air sides. As shown in Figure S12 (Supporting Information), the PL intensity of the Sn–Pb perovskites on PEDOT:PSS and SnOCl are similar when light came in from air side, but the PL density is much weaker for perovskite on PEDOT:PSS when incident light was from the ITO side.

2.2. Stability of Sn–Pb PSCs Using SnOCl

As the greatest challenge for Sn–Pb PSCs and all-perovskite tandem solar cells, their long-term stability is the most important motivation to find a proper HTM. As shown by the maximum power point (MPP) tracking stability result in **Figure** 4a, the PCE of PEDOT: PSS-based device rapidly decreased within 10 min when the device was exposed to 1 sun full spectrum illumination without cooling. However, the SnOCl-based Sn–Pb PSC did not show any decay of PCE under the same conditions

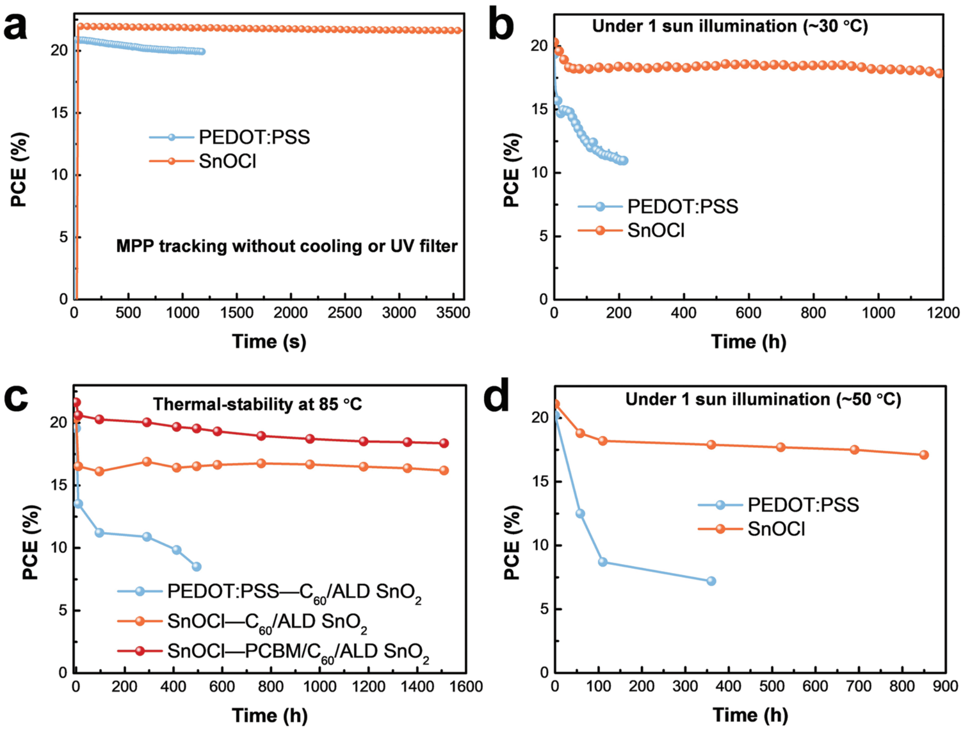

Figure 4. Enhancement of stability for Sn–Pb PSCs by using SnOCl as HTM. a) MPP tracking for Sn–Pb PSCs using PEDOT:PSS and SnOCl as HTMs, respectively. b) Long-term light stability for Sn–Pb PSCs using PEDOT:PSS and SnOCl as HTMs under one-sun illumination for 1200 h. The temperature of devices was kept at 30 °C using a cooling stage during the testing process. c) Long-term thermal stability for Sn–Pb PSCs using PEDOT:PSS and SnOCl as HTMs under a thermal stress at 85 °C for 1500 h. The tests were taken in a N_2-filled glovebox under dark. d) Long-term operation stability for Sn–Pb PSCs using PEDOT:PSS and SnOCl as HTMs under one-sun illumination without cooling for 850 h. The temperature of devices under illumination is ≈50 °C during the testing process.

after testing for 3500 s. For the long-term photostability test, the PEDOT: PSS-based device lost half of its initial PCE under one-sun illumination after testing for 100 hours while the SnOCl-based device kept over 87% of its initial PCE after light soaking for 1200 h, as shown in Figure 4b.

To pass the thermal stability test at 85 °C, the evaporated amorphous BCP layer was replaced by a robust SnO_2 layer deposited by atomic layer deposition which may prevent the ion diffusion to Cu electrode and avoid recrystallization issue of BCP. As shown in Figure 4c, the PCE of the PEDOT: PSS-based device was lost by more than 50% under 85 °C thermal stress in a N_2 environment after testing for only 100 h. Though the SnOCl-based device showed a burn-in during the initial 10 h, it kept the PCE for the following 1500 h. Although the cause for the initial burn-in effect is still unclear, we find that adding a spin-coated mixed PCBM layer between perovskite and the evaporated C_{60} layer can avoid the burn-in effect. The PCBM layer was spin-coated on a 100 °C pre-heated perovskite film and quickly annealed at 100 °C for ≈3 min to make the PCBM fully crystalized (see Experimental Section). As shown in Figure 4c, the burn-in effect was greatly suppressed, helping the devices retain 85% of the initial efficiency under 85 °C thermal stress for 1500 h. Under one sun illumination without temperature control (≈50 °C), the PEDOT:PSS based device lost ≈65% of its initial PCE after 350 h, while the SnOCl-based device still kept 81% of its initial PCE after 850 h, as shown in Figure 4d. The ternary tin (II) alloy as the HTM greatly enhanced the stability of Sn–Pb PSCs.

2.3. Hybrid Neutral PEDOT/SnOCl HTM for All-Perovskite Tandem Solar Cells

The V_{OC} of Sn–Pb perovskite devices using the SnOCl HTM is slightly lower than the best reported results,[28] which may be due to the ≈1% uncovered area of SnOCl on ITO. We employed an ultra-thin neutral PEDOT without PSS as the buffer layer between ITO and SnOCl with the device structure shown in Figure S13a (Supporting Information), so that it can fully cover ITO and also modify the work function of the ITO. This neutral PEDOT holds no potential threat to the stability of devices because of the absence of acidity. As shown in **Figure 5**a, the neutral PEDOT/SnOCl double HTMs achieved a high V_{OC} of 0.89 V, corresponding to a small V_{OC} deficit of only 0.32 V. This strategy boosted the efficiency of Sn–Pb single junction PSCs to a high value of 23.2% with a small hysteresis.

We fabricated monolithic 2-terminal all-perovskite tandem solar cells using the neutral PEDOT/SnOCl based NBG subcells and a WBG perovskite ($Cs_{0.4}FA_{0.6}PbI_{2.16}Br_{0.84}$, 1.75 eV) subcell with the device structure shown in Figure 5b and Figure S13b (Supporting Information). As shown in Figure S14a (Supporting Information) and Table 1, the WBG single-junction solar cells showed a V_{OC} of 1.22 ± 0.02 V, a J_{SC} of 17.9 ± 0.2 mA cm^{-2}, a FF of 79.4 ± 1.0% and a PCE of 17.3 ± 0.3% on average. The champion WBG device had a V_{OC} of 1.24 V, a J_{SC} of 18.1 mA cm^{-2}, a FF of 78.9%, and a PCE of 17.7% with very small hysteresis, as shown in Figure S14b (Supporting

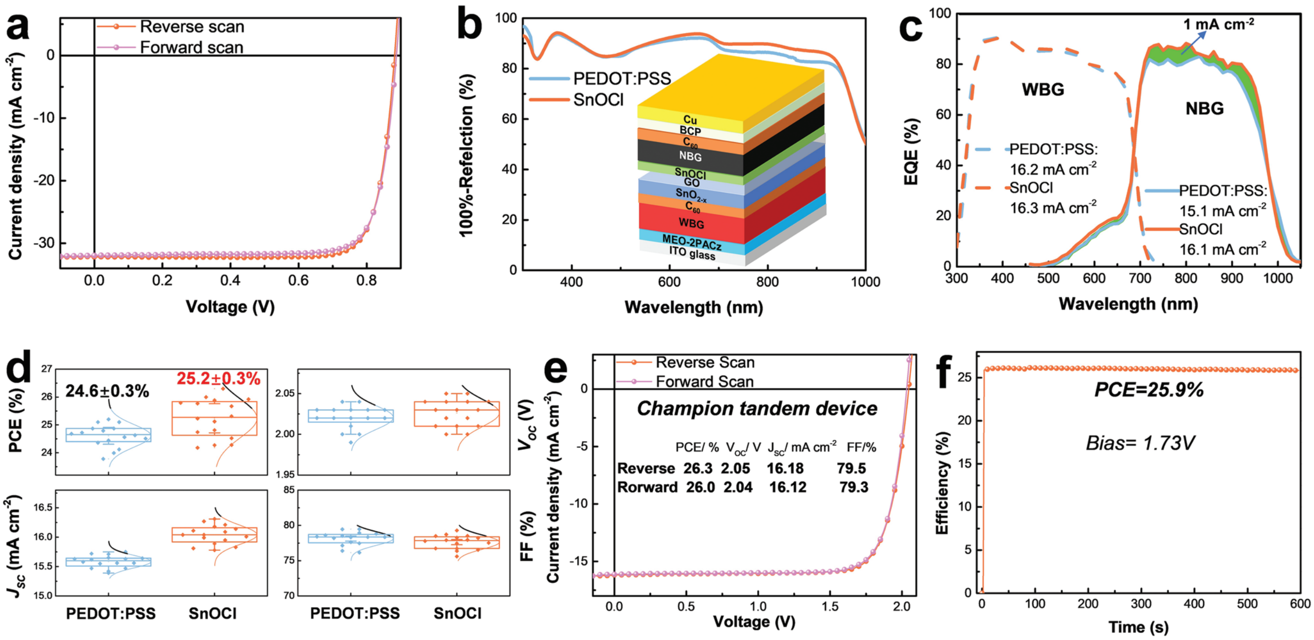

Figure 5. All-perovskite tandem solar cells with the NBG subcells using hybrid neutral PEDOT/SnOCl HTMs. a) J–V curves for the champion Sn–Pb PSC with the hybrid neutral PEDOT/SnOCl HTM under reverse and forward scanning, respectively. b) Reflection spectra for all-perovskite tandem solar cells using PEDOT:PSS and the hybrid neutral PEDOT/SnOCl HTMs for NBG subcells. The thickness of WBG subcells is the same of ≈450 nm for both kinds of devices. The tested devices with the same size (1.5 cm × 0.7 cm) are fully covered by copper electrodes. The measurements were taken using an integrating sphere. Inset is the schematic diagram of all-perovskite tandem device using the hybrid neutral PEDOT/SnOCl HTMs for NBG subcells. c) EQE spectra for the WBG and NBG subcells of the all-perovskite tandem solar cells using PEDOT:PSS and the hybrid neutral PEDOT/SnOCl HTMs, respectively. d) PV statistics for 16 all-perovskite tandem solar cells using the hybrid neutral PEDOT/SnOCl HTMs. e) J–V curves for the champion tandem device under reverse and forward scanning. f) Steady-state PCE output at the bias of 1.73 V of the champion tandem device.

Information). The integrated J_{SC} from the EQE spectrum as shown in (Figure S14c, Supporting Information) for the champion WBG device is 17.9 mA cm^{-2}, which agrees well with the J–V result. The anti-refection capability of textured SnOCl was transferred into the tandem solar cells. As shown in Figure 5b, the tandem devices using the hybrid neutral PEDOT/SnOCl HTMs have less reflection in the wavelength range from 600 to 950 nm compared with tandem devices using PEDOT:PSS. The EQE spectra of the two subcells of the tandem solar cell using PEDOT:PSS and the hybrid neutral PEDOT/SnOCl HTMs are shown in Figure 5c. The EQE spectra of WBG subcells did not notably change in the two tandem devices using the hybrid neutral PEDOT/SnOCl HTMs and PEDOT:PSS. However, the EQE of NBG subcells is obviously higher in the tandem device using the hybrid neutral PEDOT/SnOCl HTMs, which should be ascribed to both the lower optical loss and improved charge extraction efficiency. The EQE spectra for tandem device using the hybrid neutral PEDOT/SnOCl HTMs give an integrated J_{SC} of 16.3 mA cm^{-2} for the WBG subcell and 16.1 mA cm^{-2} for the NBG subcell. This is relatively well-balanced, and is close to the measured J_{SC} as shown in Figure 5d. For the tandem devices using only SnOCl as HTM, a similar enhancement of the J_{SC} from 15.7 to 16.2 mA cm^{-2} is observed compared with tandem cells using PEDOT:PSS (Figure S15, Supporting Information). The all-perovskite tandem solar cells using the hybrid neutral PEDOT/SnOCl HTMs finally achieve an averaged V_{OC} of 2.03 ± 0.02 V, a J_{SC} of 16.0 ± 0.2 mA cm^{-2}, a FF of 77.6 ± 1.0% and a PCE of 25.2 ± 0.7%. As shown in Figure 5e, the champion tandem device has a V_{OC} of 2.05 V, a J_{SC} of 16.2 mA cm^{-2}, a FF of 79.3%, and a PCE of 26.3% without notable hysteresis. The MPP tracking for the champion tandem device shows a stabilized PCE output of 25.9% for 600 s, agreeing well with J–V results, as shown in Figure 5f. As shown in Figure S16 (Supporting Information), the hybrid neutral PEDOT/SnOCl HTMs based all-perovskite tandem solar cells show greatly enhanced long-term stability, which retains 91% of the initial efficiency under one-sun illumination at ≈50 °C for 190 h.

3. Conclusion

We have reported a ternary Sn(II) alloy of SnOCl as the HTM for Sn–Pb PSCs, which successfully replaces the PEDOT:PSS, achieving boosted efficiency and stability. We found the SnOCl HTM leads to greatly enhanced J_{SC} due to the following advantages: a) reduced optical loss due to its texture structure, b) avoided the formation of small grains at the bottom of perovskite films, and c) enhanced the electron diffusion length. Benefitting from the SnOCl HTMs, a high efficiency of 22.2% was achieved for the Sn–Pb PSC. In addition, SnOCl greatly enhanced both the light and thermal stability for Sn–Pb PSCs, which retained 87% efficiency under one sun illumination for 1200 h or 85% efficiency under 85 °C thermal stress for 1500 h. The hybrid neutral PEDOT/SnOCl HTMs further boosted the efficiency of Sn–Pb PSCs over 23%, which increased the J_{SC} of all-perovskite tandem solar cells, achieving high efficiency of

≈26%. This work opened a direction for metal alloys as HTMs for Sn or Pb-based perovskites to improve the performance of the art of perovskite solar cells.

4. Experimental Section

Materials: Formamidinium iodide (FAI) was purchased from Greatcell Solar company. Lead(II) iodide (PbI_2, 99.999%), lead(II) bromide ($PbBr_2$, 99.999%), tin (II) iodide (SnI_2, 99.999%), tin (II) fluoride (SnF_2), cesium iodide (CsI, 99.999%), barium iodide (BaI_2, anhydrous, 99.995%), phenethylammonium bromide (PEABr), phenylethylamine hydrochloride (PEACl), acetone, isopropyl alcohol (IPA), toluene, anhydrous dimethyl sulfoxide (DMSO), bathocuproine (BCP), anhydrous ethyl acetate (EA), toluene, choline chloride and anhydrous *N*,*N*-dimethylformamide (DMF), chlorobenzene (CB), 1,4-diaminobutane (BDA, 99%), tin(II) chloride ($SnCl_2$, anhydrous, ≥99.99%), rubidium iodide (RbI, 99.9%), tris(pentafluorophenyl)borane (BCF), benzylhydrazine hydrochloride (BHC, 97%), 2,7-dibromo-9,9-bis[3-(dimethylamino)propyl]fluorene (DMAPF), and 8.0×10^{-3} M 4-(2,3-dihydro-1,3-dimethyl-1H-benzimidazol-2-yl)-*N*,*N*-dimethylbenzenamine (N-DMBI) were purchased from Sigma-Aldrich. MEO-2PACz (>98%) was purchased from TCI. Perfluoro(1-butenyl vinyl ether) polymer (CYTOP) was purchased from AGC company (Japan). C_{60} and [6,6]-phenyl-C_{61}-butyric acid methyl ester) (PCBM) was purchased from NANO-C company. Poly(3,4-ethyl enedioxythiophene):poly(styrene-sulfonate) PEDOT:PSS (Clevios P VP AI 4083) and neutral PEDOT (Clevios HTM Solar 3) were purchased from Heraues company. Aqueous graphene oxide (GO) solution was purchased from Graphene Supermarket. $MAPbCl_3$ single crystals were synthesized in our lab by the previously reported method.[39]

Preparation for SnOCl Precursor Solutions: 0.02–0.4 M anhydrous $SnCl_2$ was dissolved in ethyl alcohol/water (1000/1 in volume) in a N_2-filled glovebox. 1×10^{-3} M NaOH in ethyl alcohol/water (1000/1 in volume) mixed solvent was prepared to adjust the PH value of the $SnCl_2$ precursor solutions before use.

Preparation for Neutral PEDOT Solution: The purchased neutral PEDOT was diluted to 0.3-0.5 wt.% using toluene. Before use, neutral PEDOT solution was mixed with 0.5 mg mL^{-1} BCF as the dopant, then filtered with 0.22 µm poly(tetrafluoroethylene) (PTFE) filters.

Preparation for Mixed PCBM Solution: 33.0×10^{-3} M PCBM, 8.0×10^{-3} M DMAPF, and 8.0×10^{-3} M N-DMBI were dissolved in CB at RT, respectively. PCBM was prepared at stirring overnight and kept under constant stirring until solutions were used for experiments. For mixed PCBM solution preparation, PCBM, DMAPF, and NDMBI solutions were mixed in a molar ratio of 9900:56:28 and stirred overnight at RT. In this process, NDMBI and PCBM solutions were mixed and stirred for 2 h at RT, then DMAPF solution was added and continuously stirred at RT for final additives incorporated PCBM solution.

Fabrication of NBG Sn–Pb PSCs: 2.0 M $Cs_{0.2}FA_{0.8}Pb_{0.5}Sn_{0.5}I_3$ (1.21 eV) precursor solution was prepared by dissolving 1.64 M FAI, 0.41 M CsI, 1.00 M PbI_2, 1.00 M SnI_2, and 0.10 M SnF_2 in a mixed solvent (volume ratio of 1:3) of DMSO and DMF and stirred at room temperature for overnight. 2.5 mg mL^{-1} PEACl, 0.1 mol% BaI_2, 0.1 mol% RbI, and 1 mg mL^{-1} BHC (to suppress the oxidation of the Sn–Pb perovskite precursor solution)[40] were added into the precursor solution to act as additives. The perovskite solution was filtered with 0.22 µm PTFE filters before use.

ITO substrates were cleaned by ultrasonic in acetone and IPA, respectively. ITO substrates were further cleaned in a UV–ozone machine for 15 min before use. PEDOT:PSS was spin-coated onto the ITO substrates at 5000 rpm for 20 s, followed by annealing at 105 °C for 30 min in air to fabricate the PEDOT:PSS HTMs. 0.02–0.4 M $SnCl_2$ solutions were spin-coated on the cleaned ITO substrates at 4000 rpm for 60 s, followed by keeping at RT for 5 min then annealing at RT-150 °C for 10 min to fabricate the SnOCl HTMs. Then, the Sn–Pb perovskite precursor solution was spin-coated onto cleaned ITO (without HTM), PEDOT:PSS or SnOCl layer with a two-step spin-coating process: 1500 rpm for 10 s followed by 4000 rpm for 40 s. Then 150 µL EA was quickly cast on the top of perovskite 5 s before the end of the spin-coating process. Then perovskite film was annealed at 130 °C for 7 min. For surface passivation, 0.02×10^{-3} M BDA solution in toluene was cast on 5000 rpm spun perovskite films followed by annealing at 70 °C for 5 min. Finally, 25 nm C_{60}, 8 nm BCP, and 80 nm copper electrodes were sequentially thermal evaporated onto these perovskite films.

To make the Sn–Pb PSCs stabler for long-term stability testing, a 15 nm compact SnO_2 layer depositing by ALD with 210 cycles at 85 °C was fabricated between evaporated C_{60} and copper electrode layers. To suppress the burn-in effect of Sn–Pb PSCs, the mixed PCBM solution was spin-coated on the 100 °C pre-heated quickly perovskite layer at 6000 rpm for 30 s followed by annealing at 100 °C for 1 min before evaporating C_{60} layer. All the devices were sealed by a layer of CYTOP. Then the devices were covered by a glass slide, cohering with epoxy glue, and drying for overnight.

To make a hybrid neutral PEDOT/SnOCl double HTMs for Sn–Pb PSCs with higher V_{OC}, 30 µL neutral PEDOT solution was cast on a clean ITO substrate spinning at 6000 rpm for 30 s. The ultrathin neutral PEDOT layer was annealed at 100 °C for 30 min. Then the SnOCl, perovskite, C_{60}, BCP, and Cu layers were fabricated with the same method as that mentioned above.

Fabrication of WBG Perovskite Solar Cells: 1.35 M $Cs_{0.4}FA_{0.6}PbI_{2.16}Br_{0.84}$ (1.75 eV) precursor solution was prepared by dissolving 0.54 M CsI, 0.81 M FAI, 0.567 M $PbBr_2$, 0.783 M PbI_2, 4 mol% $MAPbCl_3$ single crystals, and 1.0 mg mL^{-1} PEABr in mixed solvent of DMSO and DMF (volume ratio of 3:7) and stirred at room temperature for overnight. 2×10^{-3} M MEO-2PACz in IPA was spin-coated onto ITO substrates at 6000 rpm for 20 s, followed by annealing at 100 °C for 30 min. Then, WBG perovskite precursor solution was spin-coated onto MEO-2PACz monomolecular layer at 4500 rpm. for 40 s and began to blow the films with N_2 at the 20th second of the spin-coating process. Subsequently, the samples were annealed at 120 °C for 1 min and 100 °C for 15 min. Then 1 mg mL^{-1} PEABr in IPA solution was spin-coated on the as-prepared perovskites before annealing at 100 °C for 10 min. Subsequently 1 mg mL^{-1} Choline chloride (CC) in IPA solution was spin-coated on perovskites followed by annealing at 100 °C for 30 min. Finally, 20 nm C_{60}, 8 nm BCP, and 80 nm copper electrode were sequentially thermal evaporated onto these perovskite films.

Fabrication of All-Perovskite Tandem Solar Cells: Fabricating the WBG subcells with the same process of abovementioned methods for WBG single-junction solar cells until the step of the C_{60} layer. A 15 nm compact SnO_2 layer was deposited by ALD with 210 cycles at 85 °C. Then the samples were post-annealed in air ambient at 105 °C for 30 min. Aqueous GO solution was spin-coated on the top of SnO_2 followed by annealing at 105 °C for 1 h. PEDOT:PSS or neutral PEDOT/SnOCl HTMs, Sn–Pb NBG perovskite films, C_{60}, BCP, and copper electrodes were deposited with the same process of abovementioned methods for NBG single-junction solar cells.

Electrical Measurements: Current density–voltage (*J*–*V*) measurement was performed under the simulated AM 1.5 G irradiation (100 mW cm^{-2}) produced by a xenon-lamp-based solar simulator (Oriel 94043A, 450 W AAA Solar Simulator). The light intensity was calibrated by a Reference Solar Cell and Meter (91 150, Newport). A Keithley 2400 source meter was used for the *J*–*V* measurements. All *J*–*V* measurements were taken under 100 mW cm^{-2} illumination at reverse scan mode with a scan rate of 0.05 V s^{-1}. EQE measurements were conducted with a Newport QE measurement kit by focusing a monochromatic beam of a Bruker Vertex 80v Fourier transform Interferometer with a tungsten lamp source onto the devices. Then the photocurrent was obtained through Stanford Research SR570 current preamplifier. Samples were calibrated to a Newport calibrated reference silicon solar cell with a known EQE. For tandem solar cells, light bias of blue light (≈470 nm) and infrared light (≈940 nm) with light intensity of ≈0.3 sun were used to measure the EQE of the NBG and WBG subcells, respectively. The work area of all the solar cells reported in this work unless specified is 8 mm^2, which is defined by the overlap of ITO and Cu electrodes. For an accurate measurement of device photocurrent, we applied a photomask with a smaller area of 5.9 mm^2 for all the 8 mm^2 small-area devices, as shown in each Figure caption.

Characterization—TPV and TPC Measurements: To take the TPV measurements for Sn–Pb PSCs, the devices were connected to a digital oscilloscope (DOS-X 3104A) under simulated 1-sun illumination to form an open-circuit condition (the internal impedance of the oscilloscope was set to 1 MΩ).[38] An attenuated 337 nm laser pulse (SRS NL 100 nitrogen laser, frequency of 10 Hz and pulse width of <3.5 ns.) was used as a small perturbation to the one-sun background illumination on the Sn–Pb PSCs. A photovoltage variation (ΔV) to the V_{OC} induced by the laser-pulse produced by one-sun background illumination. To take the TPC measurements for Sn–Pb PSCs, the devices were also connected to an oscilloscope and the internal impedance was set to 50 Ω to form a short-circuit condition. The same laser pulse used in TPV measurement is applied to produce a photocurrent variation (ΔI). There was no background illumination used in the TPC measurement. The carrier mobilities (μ) were calculated from the relationship of $\mu = d^2/tV_{\mathrm{bi}}$, where d, V_{bi}, and t are transit distance, built-in potential, and transit time, respectively.[41] The charge transit time was calculated to verify which layer is the limiting J_{SC} transit time. The mobility of C_{60} is ≈0.1 to 1 cm^2 V^{-1} s^{-1} and the thickness of C_{60} was only 20 nm. The carrier diffuse time through C_{60} layer was calculated to be 0.15 to 1.5 ns. The real transit time was even shorter, due to the additional built-in electric field, which is far smaller than what we measured in the TPC measurement. Thus, the electron transit time was not limited by the C_{60} layer. As the measurement of carrier mobility by TPC method needed to ensure the resistance–capacitance (*RC*) constant of the circuitry to be small enough to not limit the charge transit time determination, we controlled the *RC* constant by decreasing device capacitance to 2.4 and 1.7 ns for PEDOT:PSS and SnOCl based devices, respectively. It was realized via reducing the device active area with a laser scriber.

DLCP Measurement: The DLCP measurement for the Sn–Pb PSCs was performed by using an Agilent E4980A precision LCR meter, conducted in the DC bias scanning from 0 V to the V_{OC} (e.g., 0.9 V).[42] The AC biases was ranging from 20 to 200 mV and its frequency was ranging from 0.02–2000 kHz. The tDOS ($N_{\mathrm{T}}(E_\omega)$) is calculated as $N_{\mathrm{T}}(E_\omega) = -\frac{1}{qkT}\frac{\omega dC}{d\omega}\frac{V_{\mathrm{bi}}}{W}$, where W and V_{bi} are the depletion width and build-in potential, respectively, which were derived from the Mott–Schottky analysis of the *C*–*V* measurement. q, k, T, ω, and C are elementary charge, Boltzmann's constant, temperature, angular frequency, and specific capacitance, respectively. The demarcation energy is calculated by $E_\omega = kT\ln\left(\frac{\omega_0}{\omega}\right)$, where ω_0 is the attempt-to-escape angular frequency that is 1.0×10^{14} Hz for the $Cs_{0.2}FA_{0.8}Sn_{0.5}Pb_{0.5}I_3$ thin film. All the measurements were finished in dark conditions.

The SEM images were taken using a Hitachi S-4700 cold-cathode field-emission scanning electron microscope. Film thicknesses were measured by a Bruker Dektak XT stylus profiler. PL spectra were characterized by a Horiba iHR320 imaging spectrometer. TRPL was carried out with a PicoQuant FT300 spectrometer. A 640 nm pulsed laser with a repetition rate of 40 MHz was adopted for the measurement. XRD was carried out on a Rigaku SmartLab theta–theta diffractometer with an X-ray tube at 3.0 kW. This was configured with Cu Kα radiation (wavelength of 1.5418 Å). UV–vis–NIR absorbance and the reflection spectra were characterized by Perkin-Elmer Lambda 1050 UV–vis–NIR spectrophotometers equipped with an integrating-sphere.

Statistical Analysis: The Savitzky–Golay method was used to smoothen the data shown in Figure 1a, Figure 3c and Figure S10 (Supporting Information). The normalization was used for the data shown in Figure 3c and Figures S8, S9, S10 (Supporting Information). Data presentations of mean (averaged value) ± SD (standard deviation) shown in Figure 1c, Figure 5d, Table 1 and Figures S2, S14 (Supporting Information) refer to the PV parameter statistic for different kinds of devices. For statistical analysis shown in Figure 1c the sample size n is 15, in Figure 5d n is 16, in Figures S2 and S14 (Supporting Information) n is 12. To do the statistical analysis, the "Perform Descriptive Statistics" with Variance Divisor Moment as "DF" and the Interpolation of Quantiles as "Empirical Distribution with Averaging" were used. Origin software was used for statistical analysis in this work.

Supporting Information

Supporting Information is available from the Wiley Online Library or from the author.

Acknowledgements

This material is based upon work supported by the U.S. Department of Energy's Office of Energy Efficiency and Renewable Energy (EERE) under Solar Energy Technologies Office (SETO) Agreement Numbers DE-EE0008749. The views expressed herein do not necessarily represent the views of the U.S. Department of Energy or United States Government.

Conflict of Interest

The authors declare no conflict of interest.

Author Contributions

J.H. and Z.Y. conceived the idea. J.H. and Z.Y. designed the experiments. Z.Y. fabricated all the devices and conducted the characterizations. J.W. did the UPS, XPS, and XRD measurements and analysis. B.C. measured the EQE spectra and took the SEM images. M.A.U. prepared the mixed PCBM solution. Z.N. studied the DLCP and TRPL of Sn–Pb PSCs. G.Y. deposited the ALD SnO_2 for tandem solar cells and conducted the PL measurement. J.H. and Z.Y. wrote the paper, and all authors reviewed the paper.

Data Availability Statement

Research data are not shared.

Keywords

all-perovskite tandem solar cells, high-efficiency photovoltaics, hole-transport materials, solution-processed ternary tin (II) alloys, thermal stability, tin–lead narrow-bandgap perovskites

Received: June 24, 2022
Revised: September 21, 2022
Published online: October 31, 2022

---

[1] A. Kojima, K. Teshima, Y. Shirai, T. Miyasaka, *J. Am. Chem. Soc.* **2009**, *131*, 6050.
[2] M. M. Lee, J. Teuscher, T. Miyasaka, T. N. Murakami, H. J. Snaith, *Science* **2012**, *338*, 643.
[3] N. J. Jeon, J. H. Noh, Y. C. Kim, W. S. Yang, S. Ryu, S. I. Seok, *Nat. Mater.* **2014**, *13*, 897.
[4] W. S. Yang, J. H. Noh, N. J. Jeon, Y. C. Kim, S. Ryu, J. Seo, S. I Seok, *Science* **2015**, *348*, 1234.
[5] Q.i Jiang, Y. Zhao, X. Zhang, X. Yang, Y. Chen, Z. Chu, Q. Ye, X. Li, Z. Yin, J. You, *Nat. Photonics* **2019**, *13*, 460.
[6] NREL Best Research-Cell Efficiency Chart, https://www.nrel.gov/pv/cell-efficiency.html (accessed: June 2022).
[7] W. Chen, Y. Wu, Y. Yue, J. Liu, W. Zhang, X. Yang, H. Chen, E. Bi, I. Ashraful, M. Grätzel, L. Han, *Science* **2015**, *350*, 944.

[8] G. E. Eperon, S. D. Stranks, C. Menelaou, M. B. Johnston, L. M. Herz, H. J. Snaith, *Energy Environ. Sci.* **2014**, *7*, 982.
[9] F. Hao, C. C. Stoumpos, R. P. H. Chang, M. G. Kanatzidis, *J. Am. Chem. Soc.* **2014**, *136*, 8094.
[10] A. Sadhanala, S. Ahmad, B. Zhao, N. Giesbrecht, P. M. Pearce, F. Deschler, R. L. Z. Hoye, K. C. Godel, T. Bein, P. Docampo, S. E. Dutton, M. F. L. De Volder, R. H. Friend, *Nano Lett.* **2015**, *15*, 6095.
[11] D. P. McMeekin, G. Sadoughi, W. Rehman, G. E. Eperon, M. Saliba, M. T. Hörantner, A. Haghighirad, N. Sakai, L. Korte, B. Rech, M. B. Johnston, L. M. Herz, H. J. Snaith, *Science* **2016**, *351*, 151.
[12] G. E. Eperon, T. Leijtens, K. A. Bush, R. Prasanna, T. Green, J. T.-W. Wang, D. P. McMeekin, G. Volonakis, R. L. Milot, R. May, A. Palmstrom, D. J. Slotcavage, R. A. Belisle, J. B. Patel, E. S. Parrott, R. J. Sutton, W. Ma, F. Moghadam, B. Conings, A. Babayigit, H.-G. Boyen, S. Bent, F. Giustino, L. M. Herz, M. B. Johnston, M. D. McGehee, H. J. Snaith, *Science* **2016**, *354*, 861.
[13] K. A. Bush, A. F. Palmstrom, Z. J. Yu, M. Boccard, R. Cheacharoen, J. P. Mailoa, D. P. McMeekin, R. L. Z. Hoye, C. D. Bailie, T. Leijtens, I. M. Peters, M. C. Minichetti, N. Rolston, R. Prasanna, S. Sofia, D. Harwood, W. Ma, F. Moghadam, H. J. Snaith, T. Buonassisi, Z. C. Holman, S. F. Bent, M. D. McGehee, *Nat. Energy* **2017**, *2*, 17009.
[14] Q. Han, Y.-T. Hsieh, L. Meng, J.-.L. Wu, P. Sun, E.n-P. Yao, S.-Y. Chang, S.-H. Bae, T. Kato, V. Bermudez, Y. Yang, *Science* **2018**, *361*, 904.
[15] C.-C. Chen, S.-H. Bae, W.-H. Chang, Z. Hong, G. Li, Q. Chen, H. Zhou, Y. Yang, *Mater. Horiz.* **2015**, *2*, 203.
[16] A. Rajagopal, Z. Yang, S. B. Jo, I. L. Braly, P.-W. Liang, H. W. Hillhouse, A. K.-Y. Jen, *Adv. Mater.* **2017**, *29*, 1702140.
[17] T. Leijtens, K. A. Bush, R. Prasanna, M. D. McGehee, *Nat. Energy* **2018**, *3*, 828.
[18] D. Zhao, C. Chen, C. Wang, M. M. Junda, Z. Song, C. R. Grice, Y. Yu, C. Li, B. Subedi, N. J. Podraza, X. Zhao, G. Fang, R.-G. Xiong, K. Zhu, Y. Yan, *Nat. Energy* **2018**, *3*, 1093.
[19] R. Lin, K. Xiao, Z. Qin, Q. Han, C. Zhang, M. Wei, M. I. Saidaminov, Y. Gao, J. Xu, M. Xiao, A. Li, J. Zhu, E. H. Sargent, H. Tan, *Nat. Energy* **2019**, *4*, 864.
[20] K.e Xiao, R. Lin, Q. Han, Y. Hou, Z. Qin, H. T. Nguyen, J. Wen, M. Wei, V. Yeddu, M. I. Saidaminov, Y. Gao, X. Luo, Y. Wang, H. Gao, C. Zhang, J. Xu, J. Zhu, E. H. Sargent, H. Tan, *Nat. Energy* **2020**, *5*, 870.
[21] Z. Yu, Z. Yang, Z. Ni, Y. Shao, B. Chen, Y. Lin, H. Wei, Z. J. Yu, Z. Holman, J. Huang, *Nat. Energy* **2020**, *5*, 657.
[22] R. Lin, J. Xu, M. Wei, Y. Wang, Z. Qin, Z. Liu, J. Wu, K. Xiao, B. Chen, S. M. Park, G. Chen, H. R. Atapattu, K. R. Graham, J. Xu, J. Zhu, L. Li, C. Zhang, E. H. Sargent, H. Tan, *Nature* **2022**, *603*, 73.
[23] G. Kapil, T. Bessho, C. H. Ng, K. Hamada, M. Pandey, M. A. Kamarudin, D. Hirotani, T. Kinoshita, T. Minemoto, Q. Shen, T. Toyoda, T. N. Murakami, H. Segawa, S. Hayase, *ACS Energy Lett.* **2019**, *4*, 1991.
[24] Z. Yu, X. Chen, S. P. Harvey, Z. Ni, B. Chen, S. Chen, C. Yao, X. Xiao, S. Xu, G. Yang, Y. Yan, J. J. Berry, M. C. Beard, J. Huang, *Adv. Mater.* **2022**, *34*, 2110351.
[25] W. Ke, M. G. Kanatzidis, *Nat. Commun.* **2019**, *10*, 965.
[26] L. Lanzetta, T. Webb, N. Zibouche, X. Liang, D. Ding, G. Min, R. J. E. Westbrook, B. Gaggio, T. J. Macdonald, M. S. Islam, S. A. Haque, *Nat. Commun.* **2021**, *12*, 2853.
[27] R. Prasanna, T. Leijtens, S. P. Dunfield, J. A. Raiford, E. J. Wolf, S. A. Swifter, J. Werner, G. E. Eperon, C. de Paula, A. F. Palmstrom, C. C. Boyd, M. F. A. M. Van Hest, S. F. Bent, G. Teeter, J. J. Berry, M. D. McGehee, *Nat. Energy* **2019**, *4*, 939.
[28] S. Hu, K. Otsuka, R. Murdey, T. Nakamura, M. A. Truong, T. Yamada, T. Handa, K. Matsuda, K. Nakano, A. Sato, K. Marumoto, K. Tajima, Y. Kanemitsu, A. Wakamiya, *Energy Environ. Sci.* **2022**, *15*, 2096.
[29] B. Chen, *et al. Sci. Adv.* **2022**, add0377.
[30] Y. Chen, Z. Yang, S. Wang, X. Zheng, Y. Wu, N. Yuan, W.-H. Zhang, S. (F.) Liu, *Adv. Mater.* **2018**, *30*, 1805660.
[31] B. Cai, Y. Xing, Z. Yang, W.-H. Zhang, J. Qiu, *Energy Environ. Sci.* **2013**, *6*, 1480.
[32] D. Chi, S. Huang, M. Zhang, S. Mu, Y. Zhao, Y. Chen, J. You, *Adv. Funct. Mater.* **2018**, *28*, 1804603.
[33] C. C. Boyd, R. C. Shallcross, T. Moot, R. Kerner, L. Bertoluzzi, A. Onno, S. Kavadiya, C. Chosy, E. J. Wolf, J. Werner, J. A. Raiford, C. de Paula, A. F. Palmstrom, Z. J. Yu, J. J. Berry, S. F. Bent, Z. C. Holman, J. M. Luther, E. L. Ratcliff, N. R. Armstrong, M. D. McGehee, *Joule* **2020**, *4*, 1759.
[34] J. J. Yoo, G. Seo, M. R. Chua, T. G. Park, Y. Lu, F. Rotermund, Y.-K. Kim, C. S. Moon, N. J. Jeon, J.-P. Correa-Baena, V. Bulovic, S. S. Shin, M. G. Bawendi, J. Seo, *Nature* **2021**, *590*, 587.
[35] R. Sathyamoorthy, K. M. Abhirami, B. Gokul, S. Gautam, K. H. Chae, K. Asokan, *Electron. Mater. Lett.* **2014**, *10*, 743.
[36] B. Chen, Z. J. Yu, S. Manzoor, S. Wang, W. Weigand, Z. Yu, G. Yang, Z. Ni, X. Dai, Z. C. Holman, J. Huang, *Joule* **2020**, *4*, 850.
[37] D. Kiermasch, A. Baumann, M. Fischer, V. Dyakonov, K. Tvingstedt, *Energy Environ. Sci.* **2018**, *11*, 629.
[38] Z. Yang, Z. Yu, H. Wei, X. Xiao, Z. Ni, B. Chen, Y. Deng, S. N. Habisreutinger, X. Chen, K. Wang, J. Zhao, P. N. Rudd, J. J. Berry, M. C. Beard, J. Huang, *Nat. Commun.* **2019**, *10*, 4498.
[39] Y. Fang, Q. Dong, Y. Shao, Y. Yuan, J. Huang, *Nat. Photonics* **2015**, *9*, 679.
[40] S. Chen, X. Xiao, H. Gu, J. Huang, *Sci. Adv.* **2021**, *7*, eabe8130.
[41] Q. Jiang, Z. Chu, P. Wang, X. Yang, H. Liu, Y. Wang, Z. Yin, J. Wu, X. Zhang, J. You, *Adv. Mater.* **2017**, *29*, 1703852.
[42] Z. Ni, C. Bao, Y. Liu, Q. Jiang, W. Q. Wu, S. Chen, X. Dai, B. Chen, B. Hartweg, Z. Yu, Z. Holman, J. Huang, *Science* **2020**, *367*, 1352.